

1 A 2-dimensional Data Detrending Technique for
2 Equatorial Plasma Bubble Studies Using GOLD Far
3 Ultraviolet Observations

Rezy Pradipta¹, Chaosong Huang², and Keith M. Groves¹

Corresponding author: Rezy Pradipta, Institute for Scientific Research, Boston College,
140 Commonwealth Avenue, Chestnut Hill, MA 02467, USA (rezy.pradipta@bc.edu)

The views expressed are those of the authors and do not necessarily reflect the official policy or position of the Department of the Air Force, the Department of Defense, or the United States government. Approved for public release; distribution is unlimited. Public Affairs release approval AFRL-2023-3729.

¹Institute for Scientific Research, Boston
College, Chestnut Hill, Massachusetts, USA

²Air Force Research Laboratory, Kirtland
AFB, Albuquerque, New Mexico, USA

Key Points.

- A 2-dimensional data detrending method based on mechanical analogy of rolling a spherical ball on rough and uneven surface is formulated
- The data detrending method may be effective for revealing large-scale equatorial plasma bubble structures in 135.6 nm GOLD observation data
- Enhanced equatorial plasma bubble structures in nighttime GOLD images may be useful for development of more advanced practical applications

4 **Abstract.** We formulate a numerical data detrending technique that can
 5 be used to help reveal large-scale equatorial plasma bubble (EPB) structures
 6 in 2-dimensional data from the Global-scale Observations of the Limb and
 7 Disk (GOLD) mission. This GOLD data detrending technique is inspired by
 8 and is a generalization of a previous rolling-barrel data detrending method
 9 for 1-dimensional total electron content (TEC) observations on individual
 10 global positioning system (GPS) satellite passes. This 2-dimensional GOLD
 11 data detrending technique treats the observed 135.6 nm radiance as a func-
 12 tion of longitude and latitude as an uneven terrain, where EPBs appear as
 13 deep but narrow elongated valleys. The unperturbed background radiance
 14 is inferred by rolling a ball on the 2-dimensional terrain to skip over the EPB
 15 valleys. The two degrees-of-freedom possessed by the rolling ball allow it to
 16 smoothly trace the edges of EPB depletions, without falling into the deep
 17 valleys. Surface interpolation of radiance values at the ball's contact points
 18 onto the whole domain produces the baseline radiance. Subtracting the base-
 19 line from the original radiance data yields the net detrended radiance. As
 20 a result of the detrending, sharper contrast is present between EPB deple-

21 tions and the ambient surroundings. As such, this new 2-dimensional GOLD
22 data detrending may potentially open the door to the development of other
23 more advanced techniques for automated EPB detection and tracking, or data
24 assimilation into low-latitude space domain awareness (SDA) information
25 ecosystems.

1. Introduction

26 In the present paper, we introduce a new numerical data detrending technique that
27 can be applied to the analysis of 2-dimensional nighttime airglow data from the Na-
28 tional Aeronautics and Space Administration (NASA) Global-scale Observations of the
29 Limb and Disk (GOLD) mission [e.g. *Eastes et al.*, 2017, 2019, 2020]. The formulation
30 of this GOLD data detrending technique was motivated by the need to reliably identify
31 and track dark bands (depletions) associated with equatorial plasma bubbles (EPBs) in
32 the nighttime GOLD observations [e.g. *Karan et al.*, 2020, 2023; *Martinis et al.*, 2020;
33 *Rodriguez-Zuluaga et al.*, 2021; *Sousasantos et al.*, 2023]. Although the EPB-associated
34 depletions are often already visible in the original GOLD images, a proper data detrending
35 process will make the EPB structures significantly clearer and much more easily identi-
36 fiable. The main reason for this propensity is the fact that the low-latitude ionosphere
37 is highly inhomogeneous, with two large crests of equatorial ionization anomaly (EIA)
38 at approximately $\pm 15^\circ$ magnetic latitude on either side of the geomagnetic equator line
39 [*Appleton*, 1946; *Rishbeth*, 2000; *Balan et al.*, 2018 and references therein]. This inhom-
40 geneous plasma density configuration causes EPB structures to be highly visible at the
41 EIA crests but much less identifiable anywhere else. For this reason, data detrending can
42 be performed as a part of preliminary data processing in EPB studies [e.g. *Portillo et al.*,
43 2008; *Seemala and Valladares*, 2011; *Magdaleno et al.*, 2012; *Tang and Chen*, 2022].

44 For total electron content (TEC) data from global navigation satellite system (GNSS)
45 observations, the data detrending process is usually performed on the TEC time series
46 along individual satellite passes. In order to reveal the TEC depletions associated with

47 EPBs effectively, here one can use e.g. a special detrending technique described in *Pradipta*
48 *et al.* [2015] for the TEC data detrending process during each GPS satellite pass. The net
49 detrended Δ TEC is obtained by subtracting the inferred TEC baseline from the original
50 TEC values. The final products in the form of 2-dimensional Δ TEC maps themselves
51 are usually assembled after all the TEC data detrending process along individual GNSS
52 satellite passes have been completed. On the other hand, the situation for the GOLD data
53 is rather different because the observations inherently come in 2-dimensional form. As
54 such, an effective data detrending method with operational principles that equally match
55 the 2-dimensional nature of the GOLD measurements is desired.

56 In principle, the detrending of GOLD FUV images to reveal EPB-associated depletions
57 can also be performed using the regular 1-dimensional rolling barrel technique [*Pradipta*
58 *et al.*, 2015], as recently demonstrated by *Adkins and England* [2023]. In the aforemen-
59 tioned work [*Adkins and England*, 2023], GOLD FUV images were first transformed from
60 geographic longitude/latitude (GLON/GLAT) coordinate into quasi-dipole geomagnetic
61 (QDLON/QDLAT) coordinate, and the 1-dimensional rolling-barrel detrending technique
62 was applied consecutively for each QDLAT — one QDLAT slice at a time. A slight draw-
63 back may potentially arise in this case because the detrending process for each QDLAT
64 slice is done separately/independently of other QDLAT slices. This slice-by-slice rastering
65 could create a 2-dimensional baseline with slightly “fibrous/filamentous” texture that runs
66 along magnetic east/west orientation, unless some additional smoothing is applied. The
67 new 2-dimensional rolling-ball detrending method is intended to remedy this potential
68 issue. Here, the aforementioned issue would be avoided by the 2 degrees-of-freedom of

69 the rolling ball, which naturally incorporate data points from different LON/LAT slices
 70 at once when inferring the baseline.

71 The following sections below present a systematic description of this proposed GOLD
 72 data detrending technique. In Section 2, we describe the basic mathematical formulation
 73 and the numerical procedures for this data detrending technique. In Section 3, we provide
 74 an illustrative step-by-step working example of this data detrending procedure, and discuss
 75 a potential application of the detrended GOLD images produced by the procedure. In
 76 Section 4, we present the conclusion.

2. Basic Principles

77 Figure 1 illustrates the general idea of this new data detrending technique, which is
 78 intended for the analysis of nighttime 135.6 nm far ultraviolet (FUV) radiance data from
 79 the NASA GOLD mission. As mentioned above, the main goal of this data detrending
 80 technique is to help reveal large-scale field-aligned depletions associated with EPBs. This
 81 new data detrending technique is a 2-dimensional generalization of a similar rolling-barrel
 82 data detrending technique [Pradipta et al., 2015] that operates in 1-dimension only. In the
 83 present case, the rolling barrel is replaced with a rolling ball with two degrees of freedom
 84 to navigate an uneven 2-dimensional terrain defined by the nighttime NASA GOLD FUV
 85 airglow radiance data. Here we describe the underlying mathematical principles behind
 86 this new data detrending technique.

87 In this data detrending procedure, the GOLD FUV radiance \mathcal{R} (in Rayleighs, R) as
 88 a function of latitude Λ and longitude Φ is first transformed via variable scalings. The
 89 variable scalings are useful for creating a “terrain” with geometrical features that have
 90 comparable scale sizes in all 3 dimensions. In particular, we apply the following set

Figure 1

91 of transformations: $x = \text{longitude}/\Phi_0$; $y = \text{latitude}/\Lambda_0$; and $z = \log_{10} [(\mathcal{R} + g_0)/G_0]$.
 92 The most suitable scaling factors (determined by trial-and-error) for this purpose were
 93 $\Phi_0 = 12^\circ$, $\Lambda_0 = 5^\circ$, $g_0 = 600 \text{ R} + \min(\mathcal{R})$, and $G_0 = 0.3 \text{ R}$. In this xyz -space, the radius of
 94 the rolling ball is $R_0 = 1$ by default. This transformation compresses the dynamic range
 95 of the “terrain height” (representing the radiance values), and gives us a controlled way
 96 to select the effective size of the rolling ball relative to the terrain.

97 In the rolling-barrel detrending, we work with 1-dimensional data (e.g. TEC as a
 98 function of time) that is treated as an imaginary terrain/surface for the barrel to roll
 99 on. When encountering a valley in the terrain (i.e. depletion or negative excursion in
 100 the data), a sufficiently large barrel would be able to skip over the valley. Based on the
 101 contact points made between the barrel and the terrain/surface, this mechanical rolling
 102 motion enables us to infer a baseline that is unaffected by the presence of such valley(s).
 103 In the rolling-ball detrending, we extend the same concept for 2-dimensional case (e.g.
 104 radiance as a function of longitude and latitude). Similar to a barrel, a ball is essentially a
 105 collection of circular disks/wheels — which makes the extension of this concept possible.
 106 In Figure 1, we illustrate the geometrical configuration of such ball (with cross-sectional
 107 disks/wheels shown) on a terrain that contains some depletions. A large enough ball will
 108 be able to skip over these depletions.

109 Unlike in the 1-dimensional case of rolling-barrel detrending where only one unique
 110 circular disk is involved in the mathematical formulation, in this 2-dimensional case of
 111 rolling-ball detrending we are forced to consider not only the central wheel but also the
 112 off-center wheel(s). In Figure 1, the central wheel is shown in blue and an off-center
 113 wheel in red. This additional consideration is needed because the full mechanics of a

114 rolling ball opens the possibility for different off-center wheel(s) to make contact with the
 115 terrain, depending on the chosen direction of the roll and the exact shape of the terrain.
 116 In the diagram, the radius of an off-center wheel is denoted as R_1 and the distance of the
 117 off-center wheel from the center wheel is denoted as d_{\perp} .

118 Figure 2 shows a bird's eye view of the situation faced by the rolling ball at any given
 119 point while navigating over the terrain. The current contact point of the ball is at (x_0, y_0) ,
 120 and the roll direction is at a bearing angle φ . The immediate forward area of the roll
 121 (i.e. the "hit zone") is a circle with the same radius as the ball, placed at a forward offset
 122 such that the circle is tangential to the pivot axis line. A grid point on the terrain is
 123 highlighted as a possible next contact point (i.e. a "hit candidate"). In fact, all the grid
 124 points within the immediate forward area are considered in the contact point calculation.

Figure 2

125 In the xy -coordinate, the equation for the main line of this roll direction (aligned with
 the central wheel) is given by

$$126 \quad y = y_0 + \frac{(x - x_0)}{\tan \varphi}. \quad (1)$$

127 The distance d_{\parallel} between the pivot axis of the roll and the "hit candidate" is given by
 128 the dot product between two vectors $[x - x_0, y - y_0]$ and $[\sin \varphi, \cos \varphi]$. The first vector
 129 is pointing from the current contact point to the "hit candidate" point, and the second
 130 vector is a unit vector pointing toward the forward roll direction. This line projection via
 dot product operation yields

$$131 \quad d_{\parallel} = [x - x_0, y - y_0] \cdot [\sin \varphi, \cos \varphi] = (x - x_0) \sin \varphi + (y - y_0) \cos \varphi. \quad (2)$$

In addition, we also have the following identity:

$$132 \quad d_{\parallel}^2 + d_{\perp}^2 = (x - x_0)^2 + (y - y_0)^2, \quad (3)$$

133 as both sides of the equation equal the Euclidean distance (via the Pythagorean theorem)
 134 between the current contact point and the “hit candidate” point.

135 Figure 3 shows a diagram illustrating the basic mechanics that controls the rolling
 136 process. At each step in the rolling process, the problem is to determine which point on
 137 the terrain will be the next contact point for the ball. This is done by considering a subset
 138 of grid points on the terrain within the immediate forward-rolling zone of the ball. For
 139 each point within this area, we determine the corresponding off-center wheel that could
 140 hit the said point as the ball rolls forward. We then compute the angle $\delta \equiv \beta - \theta$ as
 141 depicted in the diagram. The grid point on the terrain with the smallest δ -angle will be
 142 the next contact point for the ball.

143 With a given d_{\perp} , the radius R_0 of the central wheel and the radius R_1 of the off-center
 144 wheel are related via $R_0^2 = R_1^2 + d_{\perp}^2$ based on the Pythagorean theorem. It means that the
 145 relation $R_1 = \sqrt{R_0^2 - d_{\perp}^2}$ holds. Here, the pivot point is at a coordinate (x_0, y_0, z_0) and
 146 the candidate for next contact point is at a coordinate (x, y, z) . For convenience, we may
 147 also define a set of increments to relate the two coordinates via $x = x_0 + \Delta x$, $y = y_0 + \Delta y$,
 148 and $z = z_0 + \Delta z$.

149 Of main interest to us is the angle $\delta \equiv \beta - \theta$, as mentioned previously. The expression
 150 for the angle θ is quite straightforward to find, which is given by

$$151 \quad \tan \theta = \frac{\Delta z}{d_{\parallel}} = \frac{\Delta z}{\Delta x \sin \varphi + \Delta y \cos \varphi}. \quad (4)$$

152 Meanwhile, the expression for the angle β requires more effort to find. Here it is useful to
 153 consider a triangle connecting the pivot axis of the roll, the ball’s main axis \mathcal{Q} , and the
 154 point \mathcal{H} on the leading edge that would land the hit. This special triangle is shown in the
 155 inset of Figure 3.

Figure 3

156 With γ defined as the complementary angle of β (i.e. $\gamma + \beta = 90^\circ$), we can apply the
 157 cosine rule in order to obtain $R_1^2 = R_0^2 + s^2 - 2R_0 s \cos \gamma = R_0^2 + s^2 - 2R_0 s \sin \beta$. Hence,
 the angle β can be expressed as

$$158 \quad \sin \beta = \frac{s^2 + R_0^2 - R_1^2}{2R_0 s}. \quad (5)$$

159 Using the known geometrical relations $s^2 = d_{\parallel}^2 + \Delta z^2$ and $R_1 = \sqrt{R_0^2 - d_{\perp}^2}$ (both come
 from the Pythagorean theorem), we can make some more simplification:

$$160 \quad \sin \beta = \frac{d_{\parallel}^2 + \Delta z^2 + R_0^2 - (R_0^2 - d_{\perp}^2)}{2R_0 \sqrt{d_{\parallel}^2 + \Delta z^2}} = \frac{(d_{\parallel}^2 + d_{\perp}^2) + \Delta z^2}{2R_0 \sqrt{d_{\parallel}^2 + \Delta z^2}}. \quad (6)$$

161 Making use of the identity $d_{\parallel}^2 + d_{\perp}^2 = (x-x_0)^2 + (y-y_0)^2 = \Delta x^2 + \Delta y^2$ (cf. Equation 3) and
 162 the expression $d_{\parallel} = (x-x_0) \sin \varphi + (y-y_0) \cos \varphi$, we can further modify the expression
 for β to yield

$$163 \quad \sin \beta = \frac{\Delta x^2 + \Delta y^2 + \Delta z^2}{2R_0 \sqrt{(\Delta x \sin \varphi + \Delta y \cos \varphi)^2 + \Delta z^2}}. \quad (7)$$

Hence the complete expression for the angle $\delta \equiv \beta - \theta$ is given by

$$164 \quad \delta = \sin^{-1} \left[\frac{\Delta x^2 + \Delta y^2 + \Delta z^2}{2R_0 \sqrt{(\Delta x \sin \varphi + \Delta y \cos \varphi)^2 + \Delta z^2}} \right] - \tan^{-1} \left[\frac{\Delta z}{\Delta x \sin \varphi + \Delta y \cos \varphi} \right]. \quad (8)$$

165 For all the terrain points located within the ball's immediate forward-rolling zone, we
 166 must find one with the smallest δ -angle in order to determine the next contact point for
 167 the rolling ball.

168 Using the aforementioned basic mechanics, we will roll the ball around the whole terrain
 169 in xy -space and mark the contact points. We will then take the radiance values at the
 170 contact points and interpolate them onto the entire terrain grid. This interpolation will
 171 establish the baseline radiance level that excludes the EPB depletions — i.e. an essentially
 172 “depletion-free” baseline radiance. Subtracting this baseline from the original data will
 173 give us the net radiance values and reveal the EPB depletions with greater clarity.

3. Illustrative Examples

Figure 4 shows a working example of this data detrending process. Figure 4a shows the original 135.6 nm GOLD FUV radiance data (in geographic latitude/longitude coordinate) from observations made on 2 February 2022 at 21:40 UTC. The dynamic range of the observed radiance value is generally between 0 R and 2500 R, with higher radiance values coming from the crests of the equatorial ionization anomaly (EIA). The EIA crests may also exhibit some variations that are recognizable in the GOLD FUV data [Eastes et al., 2023]. A number of EPB-related depletions are already visible in the data, and EPB analysis could be performed with these original GOLD images [e.g. Aa et al., 2020]. However, these depletions can be enhanced further by the data detrending. Figure 4b shows the result of rastering process by the rolling ball as it navigates around the terrain in the xy -space. White circle indicates the size of the ball, and magenta dots mark the ball's contact points. The rastering process begins at the highest point on the terrain, and we start rolling the ball toward a randomly selected direction at an initial bearing angle $\varphi = \varphi_0$. After each roll, we vary the bearing angle φ by a random variable uniformly distributed between $\pm\Delta\varphi$. The magnitude of this “scattering amplitude” is initially set to be quite small at $\Delta\varphi = 20^\circ$, which remains constant while the number of executed rolls are still below 20% of the total number of grid points in the terrain. After that, we progressively increase the magnitude of $\Delta\varphi$ by an additional 10° when the number of executed rolls reach 20%, 40%, 60%, and 80% of the total number of grid points in the terrain, respectively. This randomized “scatter-after-each-roll” policy is intended to prevent the ball from being accidentally trapped in a closed loop. When the ball arrives at the outer boundary, it will be turned back toward the interior of the computational

Figure 4

196 domain, at a new randomly selected bearing angle. The rastering process ends when the
 197 number of executed rolls reach the total number of grid points in the terrain. A few
 198 additional plots illustrating more details on the progression of the rolling-ball rastering
 199 process are provided in the Supplementary Material.

200 Figure 4c depicts the 2-dimensional baseline radiance level, obtained by interpolating
 201 the radiance values at the contact points onto the whole terrain grid (in regular geographic
 202 latitude/longitude coordinate). A bilinear numerical interpolation was used for computing
 203 the baseline radiance level. Higher background radiance values are naturally found at the
 204 two EIA crests, consistent with the $\sim n_e^2$ dependence of the 135.6 nm OI volume emission
 205 rate from ionospheric F-region altitudes, where n_e is the electron density [*Tinsley and*
 206 *Bittencourt, 1975; Melendez-Alvira et al., 1999; Qin et al., 2015*]. Finally, Figure 4d
 207 shows the 2-dimensional net radiance profile that was obtained by subtracting the inferred
 208 baseline level from the original radiance data (expressed in geographic latitude/longitude
 209 coordinate). The typical dynamic range of the net detrended radiance value is between
 210 -1000 R and 100 R, with deeper depletions generally occurring around the EIA crest
 211 locations. In the net radiance data, sharper contrast is present between EPB-associated
 212 depletions and the unperturbed regions. This enhanced contrast may help significantly in
 213 terms of EPB detection, either visually or computationally, compared to working directly
 214 with the original radiance data.

215 The depth of the elongated depletions in detrended GOLD images may be used to
 216 quantify the intensity of EPBs. This concept is aligned with an analysis conducted by
 217 *Aa et al. [2023]*, in which the differential radiance $\Delta\mathcal{R}$ was obtained by subtracting a
 218 running average baseline. The standard deviation of normalized $\Delta\mathcal{R}$ was then used as

219 a Bubble Index to quantify the EPB intensity. In the future, the same could be tried
220 with $\Delta\mathcal{R}$ obtained using the present rolling-ball detrending technique, which may offer
221 some improvement since the EPBs would be more accurately manifested as depletions
222 (i.e. negative excursions) in $\Delta\mathcal{R}$ rather than large-amplitude oscillatory signals (with
223 both hills and valleys).

224 Other, more advanced applications may also be developed based on the enhanced EPB
225 features observed in the net detrended GOLD FUV images. An example of such applica-
226 tion is a 3-dimensional volumetric representation of the large-scale EPB structures. Here
227 we provide a basic conceptual illustration of this particular potential usage of the net
228 detrended GOLD FUV images.

229 Figure 5 shows a case example to illustrate this potential application. Figure 5a displays
230 a detrended GOLD image on 2 February 2022 at 00:22 UTC, which shows a sequence of
231 large-scale EPB depletion structures between 80°W - 20°W longitude. Enhanced by the
232 data detrending process, some branching/bifurcations are also revealed at the tips of
233 these EPB structures. Figure 5b displays the same detrended GOLD image, but with
234 the skeletons/spines of the observed EPB structures added as green line segments on the
235 image. For the purpose of this illustrative example, these EPB spines were determined
236 by manually profiling the observed EPB structures in the detrended GOLD image. In
237 the future, automated profiling of complex EPB spines might potentially be achievable
238 through computational algorithm(s). The profiled EPB spines will be a key ingredient for
239 assembling the 3-dimensional volumetric representation.

240 Figure 5c shows a visualization plot containing two planar projections of the EPB
241 structures, one along a horizontal plane at 300 km altitude (nominally taken as the 135.6

242 nm OI emission source height) and the other along a vertical E/W plane at 5°S latitude.
243 Magenta dots at $z = 0$ km are the shadow of the EPB plume structures projected onto
244 ground level. For visualization purposes, we assume that the plasma density is fully
245 depleted at the spine lines. In the neighborhood of each spine line, the depletion is
246 set to subside as a function of distance following a bivariate Gaussian profile with a
247 standard deviation of $\sigma = 0.25^\circ$ in latitude/longitude. In the far-field away from any spine
248 line, there is practically no depletion in plasma density. The simplified depletion profiles
249 were subsequently projected along the geomagnetic field lines using the International
250 Geomagnetic Reference Field (IGRF) model [*Thebault et al., 2015; Alken et al., 2021*].
251 On the two planar projections, the relative plasma density values (Rel. N_e) are indicated
252 with colormap.

253 Figure 5d shows a similar visualization plot, this time displaying a 3-dimensional volu-
254 metric representation of the observed EPB structures. Here, the 3-dimensional morphol-
255 ogy of the EPBs (which resemble a series of arches) is represented using isosurface at Rel.
256 $N_e = 0.6$ level. The alpha color transparency was set at 0.15 to make the isosurfaces
257 translucent. The depleted part of ionospheric plasma is essentially the volume contained
258 within the arches. The arches are elongated roughly along the N/S direction, turned
259 slightly sideways following the magnetic declination angle. Like in Figure 5c, magenta
260 dots at $z = 0$ km are the shadow of these arches projected onto ground level. This volu-
261 metric representation illustrates how the EPB-associated magnetic flux tubes occupy the
262 3-dimensional space.

263 Animations that provide additional perspectives on the visualization shown in Figure 5d,
264 viewing the 3-dimensional volumetric structures dynamically from different angles, are
265 included in the Supplementary Material.

266 For a more comprehensive data assimilation, similar concept can be applied but a few
267 aspects need to be modified. Aspects that would be subject to modifications are as
268 follows. (1) The numerical value of relative depletions at the spine lines will have to be
269 determined empirically from the net radiance and baseline radiance data arrays. (2) The
270 process will no longer be only about the relative level of depletions, but the end result is
271 going to be expressed in terms of ionospheric plasma density and/or TEC values. (3) The
272 background plasma density and/or TEC may be obtained from ionosphere models such
273 as IRI, NeQuick, NET, TIE-GCM, or WAM-IPE [*Coisson et al.*, 2006; *Nava et al.*, 2008;
274 *Quan et al.*, 2014; *Bilitza et al.*, 2022; *Fang et al.*, 2018; *Smirnov et al.*, 2023]. Aside from
275 these few modifications, the process would be quite straightforward: the relative depletion
276 profile is going to be stamped onto the smooth background plasma density and/or TEC
277 profile. This procedure will produce a model ionosphere that contains a representation of
278 the EPB plume structures.

279 In the conceptual example discussed above, the 3-dimensional volumetric representa-
280 tion of EPB structures may potentially have its practical usage in the context of space
281 situational awareness (SSA) and space domain awareness (SDA) information ecosystems.
282 This potential usage might be directed toward actual implementation if the SSA/SDA
283 system has a focus on low-latitude regions, and concerns not only the physical survivabil-
284 ity of space assets in orbit but also their state of radio connectivity in VHF/UHF bands

285 to various terrestrial components [e.g. *Bishop et al.*, 2004; *Belehaki et al.*, 2015; *Mendillo*
286 *et al.*, 2018; *Bahar et al.*, 2022].

4. Conclusion

287 We have formulated a new 2-dimensional data detrending method that can be used in
288 the analysis of nighttime GOLD FUV emission data to help reveal large-scale EPB struc-
289 tures. A generalization of a previous GPS TEC data detrending technique in 1-dimension
290 [*Pradipta et al.*, 2015], this new GOLD data detrending method works by a mechanical
291 analogy of rolling a spherical ball on an uneven terrain surface. The rolling ball's ability
292 to skip over EPB-associated depletions (deep-but-narrow valleys in the terrain surface)
293 allows the data detrending method to deduce suitable baseline level to exclude the EPBs.
294 The detrending process enhances the contrast between EPB depletions and the ambient
295 surroundings, making the detrended GOLD images a powerful resource for those conduct-
296 ing EPB research in the South American and Atlantic sectors.

297 Another objective carried by the proposed GOLD FUV data detrending method is to
298 enable and/or facilitate the development of other, more advanced applications. We have
299 discussed a conceptual example of such potential applications, involving 3-dimensional
300 volumetric representation of EPB structures over a wide range of longitudes. The given
301 example highlights the potential utility of assimilating detrended GOLD FUV images into
302 SSA/SDA information ecosystems. Future work will be directed toward exploring other
303 potential applications of the 2-dimensional GOLD data detrending method. It is hoped
304 that many practical applications using detrended GOLD images (or airglow images more
305 generally) can be realized in the future.

5. Open Research

306 The NASA GOLD Level 1C observation datafiles for this study are available from the
307 GOLD mission webpage at <https://gold.cs.ucf.edu/data/> or from the NASA Space
308 Physics Data Facility webpage at <https://spdf.gsfc.nasa.gov/pub/data/gold/level1c/>.

309 **Acknowledgments.** This work was supported by the NASA GOLD-ICON Guest In-
310 vestigators (GIGI) program under grant #NNH22OB17A.

311 **Disclaimer:** The views expressed are those of the authors and do not necessarily
312 reflect the official policy or position of the Department of the Air Force, the Department
313 of Defense, or the U.S. government.

References

- 314 Aa, E., Zou, S., Eastes, R., Karan, D. K., Zhang, S.-R., Erickson, P. J., and Coster,
315 A. J. (2020), Coordinated ground-based and space-based observations of equatorial
316 plasma bubbles, *Journal of Geophysical Research: Space Physics*, 125, e2019JA027569,
317 <https://doi.org/10.1029/2019JA027569>.
- 318 Aa, E., Zhang, S.-R., Liu, G., Eastes, R. W., Wang, W., Karan, D. K., et al. (2023),
319 Statistical analysis of equatorial plasma bubbles climatology and multi-day period-
320 icity using GOLD observations, *Geophysical Research Letters*, 50, e2023GL103510,
321 <https://doi.org/10.1029/2023GL103510>.
- 322 Adkins, V. J., and England, S. L. (2023), Automated detection and tracking of
323 equatorial plasma bubbles utilizing Global-Scale Observations of the Limb and
324 Disk (GOLD) 135.6 nm Data, *Earth and Space Science*, 10, e2023EA002935,
325 <https://doi.org/10.1029/2023EA002935>.

- 326 Alken, P., Thebault, E., Beggan, C. D., et al. (2021), International Geomag-
327 netic Reference Field: the thirteenth generation, *Earth Planets Space*, 73, 49,
328 <https://doi.org/10.1186/s40623-020-01288-x>.
- 329 Appleton, E. V. (1946), Two anomalies in the ionosphere, *Nature*, 157, 691,
330 <https://doi.org/10.1038/157691a0>.
- 331 Bahar, A., Dear, V., Husin, A., Faturahman, A., Harjosuwito, J., and Pradipta, R.
332 (2022), Exploring an Extension of Space Situational Awareness in Southeast Asian
333 Region Utilizing EAR Observation Data, In: Yulihastin, E., Abadi, P., Sitom-
334 pul, P., Harjupa, W. (eds), Proceedings of the International Conference on Radio-
335 science, Equatorial Atmospheric Science and Environment and Humanosphere Science
336 (INCREASE) 2021, *Springer Proceedings in Physics*, vol 275, Springer, Singapore,
337 https://doi.org/10.1007/978-981-19-0308-3_21.
- 338 Balan, N., Liu, L. and Le, H. (2018), A brief review of equatorial ionization
339 anomaly and ionospheric irregularities, *Earth and Planetary Physics*, 2: 257-275,
340 <https://doi.org/10.26464/epp2018025>.
- 341 Belehaki, A., Tsagouri, I., Kutiev, I., Marinov, P., Zolesi, B., Pietrella, M., Themelis, K.,
342 Elias, P., and Tziotziou, K. (2015), The European Ionosonde Service: nowcasting and
343 forecasting ionospheric conditions over Europe for the ESA Space Situational Awareness
344 services, *J. Space Weather Space Clim.*, 5, A25, <https://doi.org/10.1051/swsc/2015026>.
- 345 Bilitza, D., Pezzopane, M., Truhlik, V., Altadill, D., Reinisch, B. W., and Pignal-
346 beri, A. (2022), The International Reference Ionosphere model: A review and de-
347 scription of an ionospheric benchmark, *Reviews of Geophysics*, 60, e2022RG000792,
348 <https://doi.org/10.1029/2022RG000792>.

- 349 Bishop, G., Bullett, T. W., Groves, K. M., Quigley, S., Doherty, P. H., Sexton, E., Scro,
350 K., Wilkes, R., and Citrone, P. (2004), Operational Space Environment Network Display
351 (OpSEND), *Radio Sci.*, 39, RS1S26, <https://doi.org/10.1029/2002RS002836>.
- 352 Coisson, P., S. M. Radicella, R. Leitinger, and B. Nava (2006), Topside electron den-
353 sity in IRI and NeQuick: Features and limitations, *Adv. Space Res.*, 37(5), 937-942,
354 <https://doi.org/10.1016/j.asr.2005.09.015>.
- 355 Eastes, R. W., McClintock, W. E., Burns, A. G., Anderson, D. N., Andersson, L., Co-
356 drescu, M., Correira, J. T., Daniell, R. E., England, S. L., Evans, J. S., Harvey, J.,
357 Krywonos, A., Lumpe, J. D., Richmond, A. D., Rusch, D. W., Siegmund, O., Solomon,
358 S. C., Strickland, D. J., Woods, T. N., Aksnes, A., Budzien, S. A., Dymond, K. F.,
359 Eparvier, F. G., Martinis, C. R., and Oberheide, J. (2017), The Global-scale Observa-
360 tions of the Limb and Disk (GOLD) mission, *Space Science Reviews*, 212(1-2), 383-408,
361 <https://doi.org/10.1007/s11214-017-0392-2>.
- 362 Eastes, R. W., Solomon, S. C., Daniell, R. E., Anderson, D. N., Burns, A. G., England,
363 S. L., et al. (2019), Global-scale observations of the equatorial ionization anomaly,
364 *Geophysical Research Letters*, 46, 9318-9326, <https://doi.org/10.1029/2019GL084199>.
- 365 Eastes, R. W., McClintock, W. E., Burns, A. G., Anderson, D. N., Andersson, L., Aryal,
366 S., et al. (2020), Initial observations by the GOLD mission, *Journal of Geophysical*
367 *Research: Space Physics*, 125, e2020JA027823, <https://doi.org/10.1029/2020JA027823>.
- 368 Eastes, R. W., Karan, D. K., Martinis, C., Daniell, R. E., Gan, Q., Burns, A. G., and Mc-
369 Clintock, W. E. (2023), GOLD observations of longitudinal variations in the nighttime
370 equatorial ionization anomaly (EIA) crests' latitudes, *Journal of Geophysical Research:*
371 *Space Physics*, 128, e2022JA031007, <https://doi.org/10.1029/2022JA031007>.

372 Fang, T.-W., Fuller-Rowell, T., Yudin, V., Matsuo, T., and Viereck, R. (2018), Quanti-
373 fying the sources of ionosphere day-to-day variability, *Journal of Geophysical Research:*
374 *Space Physics*, 123, 9682-9696, <https://doi.org/10.1029/2018JA025525>.

375 Karan, D. K., Daniell, R. E., England, S. L., Martinis, C. R., Eastes, R. W.,
376 Burns, A. G., and McClintock, W. E. (2020), First zonal drift velocity mea-
377 surement of equatorial plasma bubbles (EPBs) from a geostationary orbit using
378 GOLD data, *Journal of Geophysical Research: Space Physics*, 125, e2020JA028173,
379 <https://doi.org/10.1029/2020JA028173>.

380 Karan, D. K., Eastes, R. W., Daniell, R. E., Martinis, C. R., and McClintock,
381 W. E. (2023), GOLD mission's observation about the geomagnetic storm effects
382 on the nighttime equatorial ionization anomaly (EIA) and equatorial plasma bub-
383 bles (EPB) during a solar minimum equinox, *Space Weather*, 21, e2022SW003321,
384 <https://doi.org/10.1029/2022SW003321>.

385 Magdaleno, S., Herraiz, M., and Radicella, S. M. (2012), Ionospheric bubble seeker:
386 A java application to detect and characterize ionospheric plasma depletion from
387 GPS data, *IEEE Transactions on Geoscience and Remote Sensing*, 50(5), 1719-1727,
388 <https://doi.org/10.1109/TGRS.2011.216896>.

389 Martinis, C., Daniell, R., Eastes, R., Norrell, J., Smith, J., Klenzing, J., et al. (2021),
390 Longitudinal variation of postsunset plasma depletions from the global-scale observa-
391 tions of the limb and disk (GOLD) mission, *Journal of Geophysical Research: Space*
392 *Physics*, 126, e2020JA028510, <https://doi.org/10.1029/2020JA028510>.

393 Melendez-Alvira, D. J., Meier, R. R., Picone, J. M., Feldman, P. D., and McLaughlin,
394 B. M. (1999), Analysis of the oxygen nightglow measured by the Hopkins Ultraviolet

395 Telescope: Implications for ionospheric partial radiative recombination rate coefficients,
396 *J. Geophys. Res.*, 104(A7), 14901-14913, <https://doi.org/10.1029/1999JA900136>.

397 Mendillo, M., Hickey, D., Martinis, C., Wroten, J., and Baumgardner, J.
398 (2018), Space weather nowcasting for area-denied locations: Testing all-sky imag-
399 ing applications at geomagnetic conjugate points, *Space Weather*, 16, 47-56,
400 <https://doi.org/10.1002/2017SW001741>.

401 Nava, B., P. Coisson, and S. M. Radicella (2008), A new version of the NeQuick ionosphere
402 electron density model, *J. Atmos. Sol. Terr. Phys.*, 70(15), 1856-1862.

403 Portillo, A., Herraiz, M., Radicella, S. M., and Ciruolo, L. (2008), Equato-
404 rial plasma bubbles studied using African slant total electron content obser-
405 vations, *Journal of Atmospheric and Solar-Terrestrial Physics*, 70(6), 907-917,
406 <https://doi.org/10.1016/j.jastp.2007.05.019>.

407 Pradipta, R., Valladares, C. E., and Doherty, P. H. (2015), An effective TEC
408 data detrending method for the study of equatorial plasma bubbles and travel-
409 ing ionospheric disturbances, *J. Geophys. Res. Space Physics*, 120, 11,048-11,055,
410 <https://doi.org/10.1002/2015JA021723>.

411 Qin, J., Makela, J. J., Kamalabadi, F., and Meier, R. R. (2015), Radiative transfer
412 modeling of the OI 135.6 nm emission in the nighttime ionosphere, *J. Geophys. Res.*
413 *Space Physics*, 120, 10116-10135, <https://doi.org/10.1002/2015JA021687>.

414 Qian, L., Burns, A.G., Emery, B.A., Foster, B., Lu, G., Maute, A., Richmond,
415 A.D., Roble, R.G., Solomon, S.C. and Wang, W. (2014), The NCAR TIE-GCM:
416 A Community Model of the Coupled Thermosphere/Ionosphere System, In *Modeling*
417 *the Ionosphere-Thermosphere System* (eds J. Huba, R. Schunk and G. Khazanov),

- 418 <https://doi.org/10.1002/9781118704417.ch7>.
- 419 Rishbeth, H. (2000), The equatorial F-layer: Progress and puzzles, *Ann. Geophys.*, 18,
420 730, <https://doi.org/10.1007/s00585-000-0730-6>.
- 421 Rodriguez-Zuluaga, J., Stolle, C., Yamazaki, Y., Xiong, C., and England, S. L. (2021), A
422 synoptic-scale wavelike structure in the nighttime equatorial ionization anomaly, *Earth
423 and Space Science*, 8, e2020EA001529, <https://doi.org/10.1029/2020EA001529>.
- 424 Seemala, G. K., and Valladares, C. E. (2011), Statistics of total electron content depletions
425 observed over the South American continent for the year 2008, *Radio Sci.*, 46, RS5019,
426 <https://doi.org/10.1029/2011RS004722>.
- 427 Smirnov, A., Shprits, Y., Prol, F. et al. (2023), A novel neural network model of Earth's
428 topside ionosphere, *Sci Rep*, 13, 1303, <https://doi.org/10.1038/s41598-023-28034-z>.
- 429 Sousasantos, J., Gomez Socola, J., Rodrigues, F.S., et al. (2023), Severe L-band scintil-
430 lation over low-to-mid latitudes caused by an extreme equatorial plasma bubble: joint
431 observations from ground-based monitors and GOLD, *Earth Planets Space*, 75, 41,
432 <https://doi.org/10.1186/s40623-023-01797-5>.
- 433 Tang, L., and Chen, G. (2022), Equatorial plasma bubble detection using
434 vertical TEC from altimetry satellite, *Space Weather*, 20, e2022SW003142,
435 <https://doi.org/10.1029/2022SW003142>.
- 436 Thebault, E., Finlay, C. C., Beggan, C. D., et al. (2015), International Ge-
437 omagnetic Reference Field: the 12th generation, *Earth Planet Sp*, 67, 79,
438 <https://doi.org/10.1186/s40623-015-0228-9>.
- 439 Tinsley, B. A., and Bittencourt, J. A. (1975), Determination of F region height and peak
440 electron density at night using airglow emissions from atomic oxygen, *J. Geophys. Res.*,

441 80(16), 2333-2337, <https://doi.org/10.1029/JA080i016p02333>.

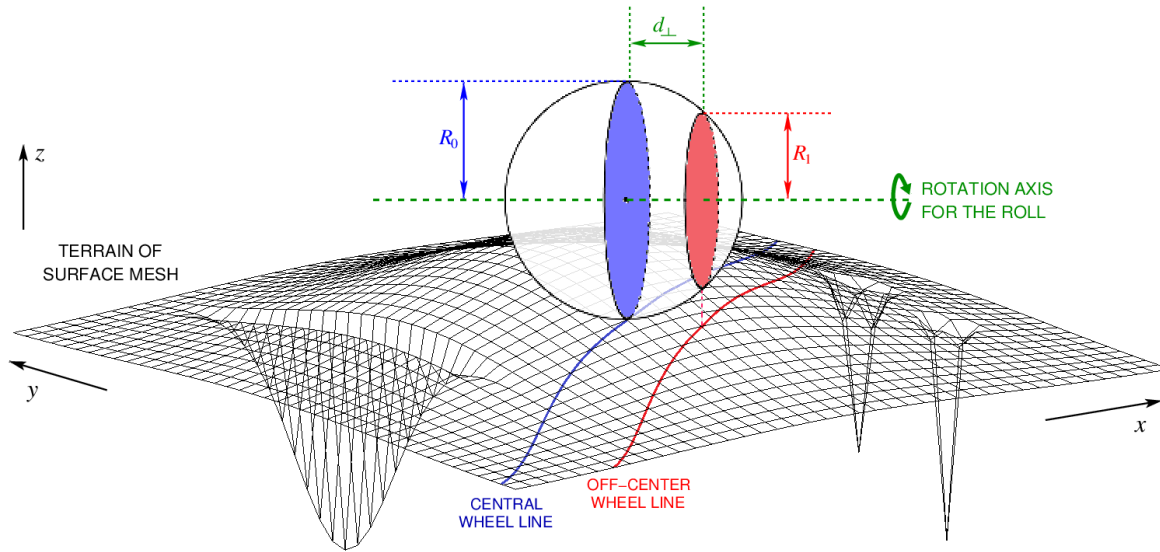


Figure 1. Graphical illustration of 2-dimensional data detrending process using mechanical analogy of a rolling ball on an uneven terrain. A ball with sufficiently large radius should be able to skip/roll over deep-but-narrow valleys, which correspond to EPB depletions in the case of GOLD FUV data.

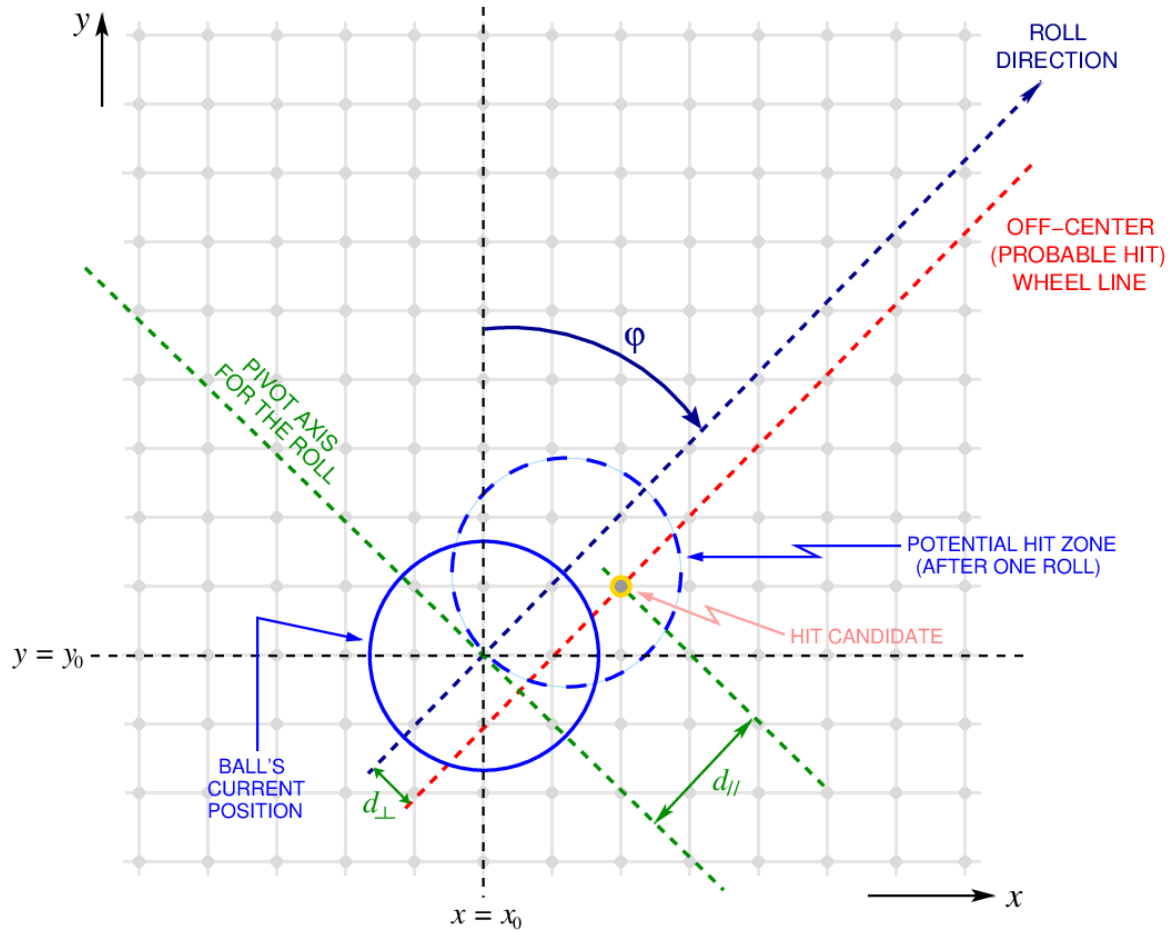


Figure 2. Bird's eye view of the rolling ball on the terrain grid, showing the starting position of the ball (solid circle), the chosen roll direction (at bearing angle ϕ relative to the y -axis), and the potential hit zone (dashed circle) where one of the grid points would make contact with the ball next.

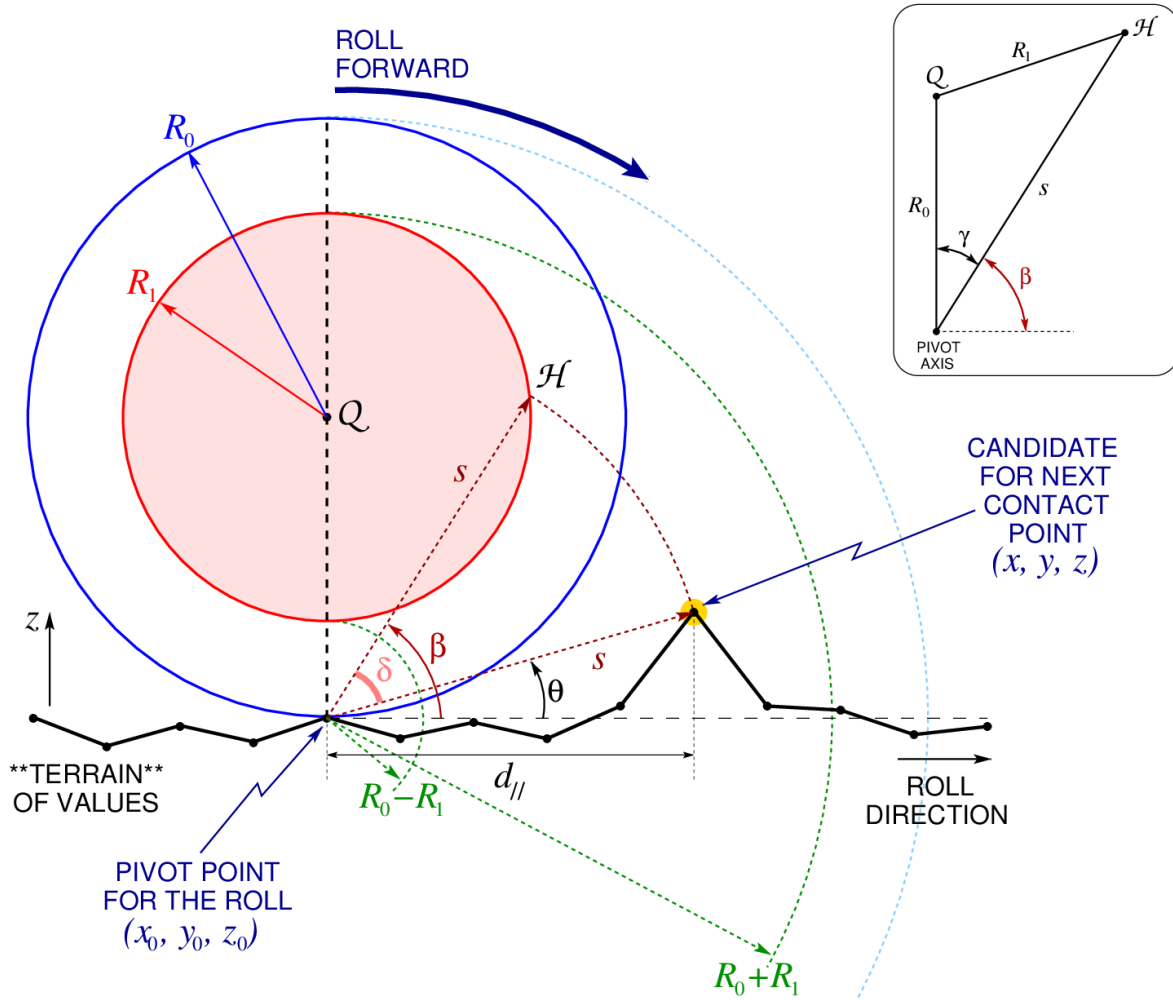


Figure 3. Detailed cross-sectional sideways view of the rolling ball, with one of the grid points on the terrain under focus as a contact candidate. The corresponding off-center wheel (shaded circle) in alignment with the said gridpoint is shown, where potential contact may happen at the point marked \mathcal{H} . Determining the next contact point of the rolling ball is equivalent to finding the grid point with the smallest δ -angle to its corresponding wheel.

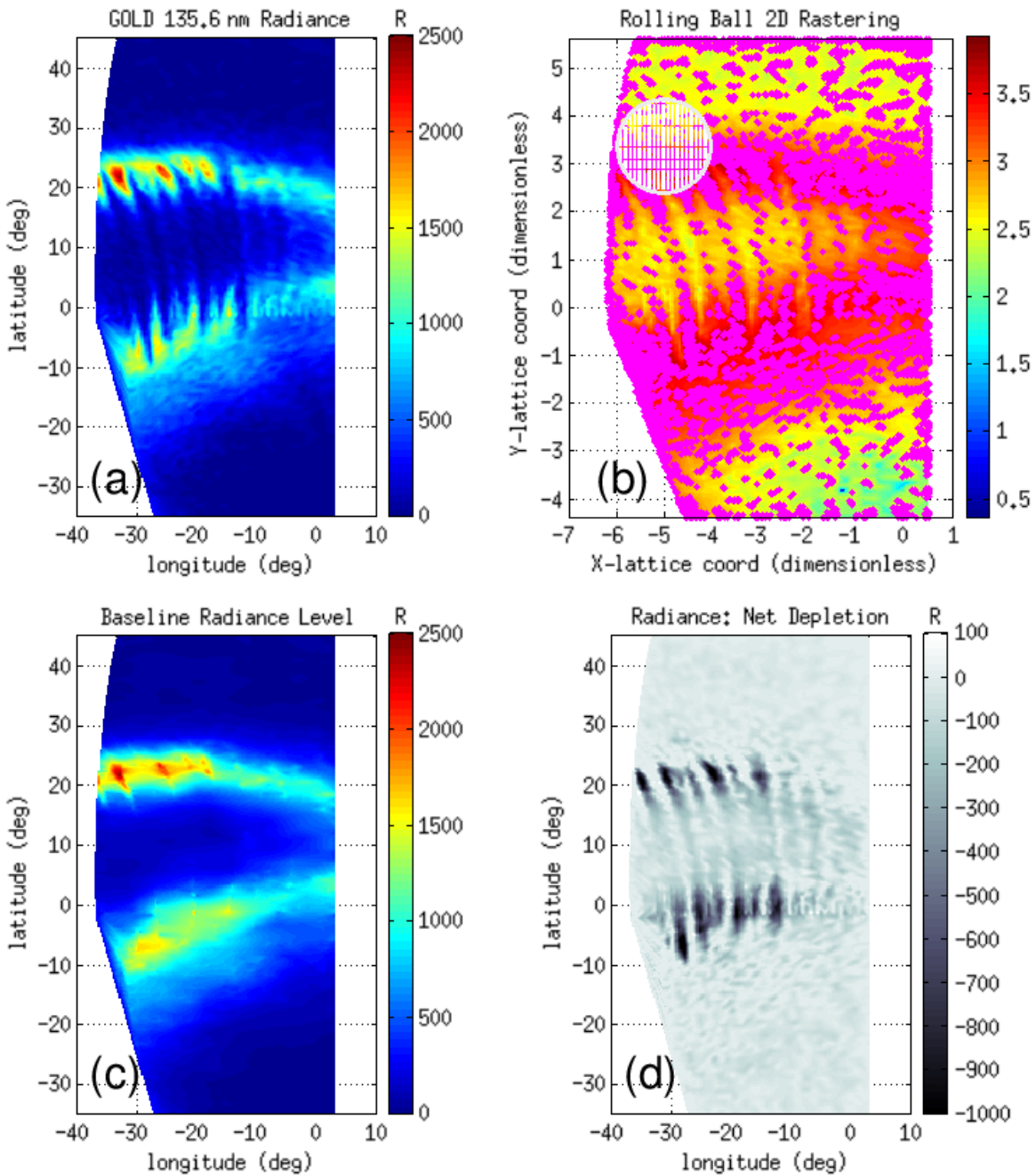


Figure 4. Step-by-step working illustration of the data detrending procedure. (a) Original GOLD radiance data. (b) Navigation/rastering process by the rolling ball over the proverbial terrain. (c) Baseline level obtained by interpolating radiance values at the contact points onto the whole grid. (d) Net radiance values obtained by subtracting the baseline from the original GOLD data.

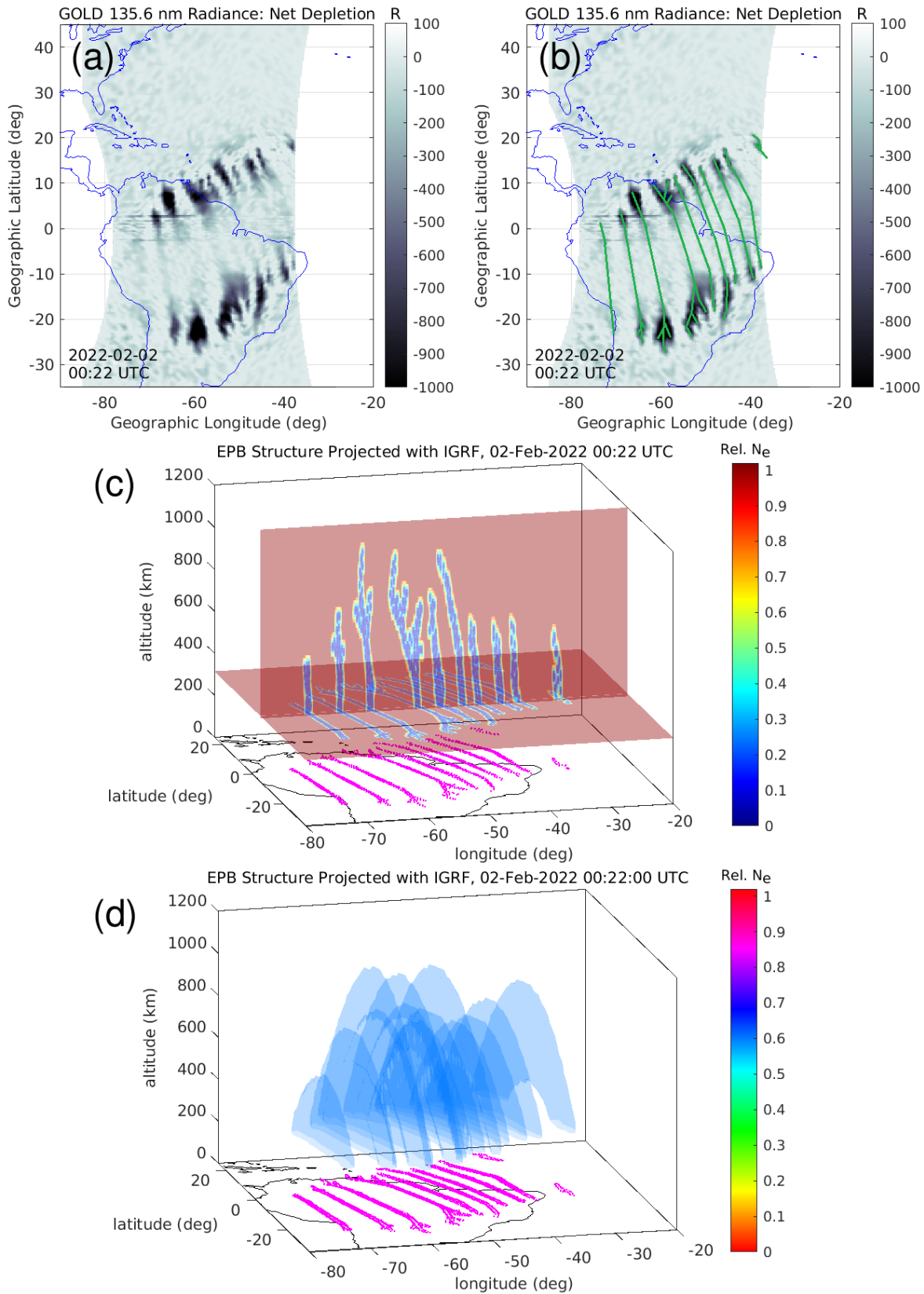


Figure 5. (a) Detrended GOLD image on 2 February 2022 at 00:22 UTC, showing several large-scale EPB structures. (b) The same GOLD image with skeletons/spines of the EPB structures profiled. (c) Horizontal and vertical planar projections of the observed EPB structures using IGRF. (d) A 3-dimensional volumetric representation of the observed EPB structures using IGRF.

Figure 1.

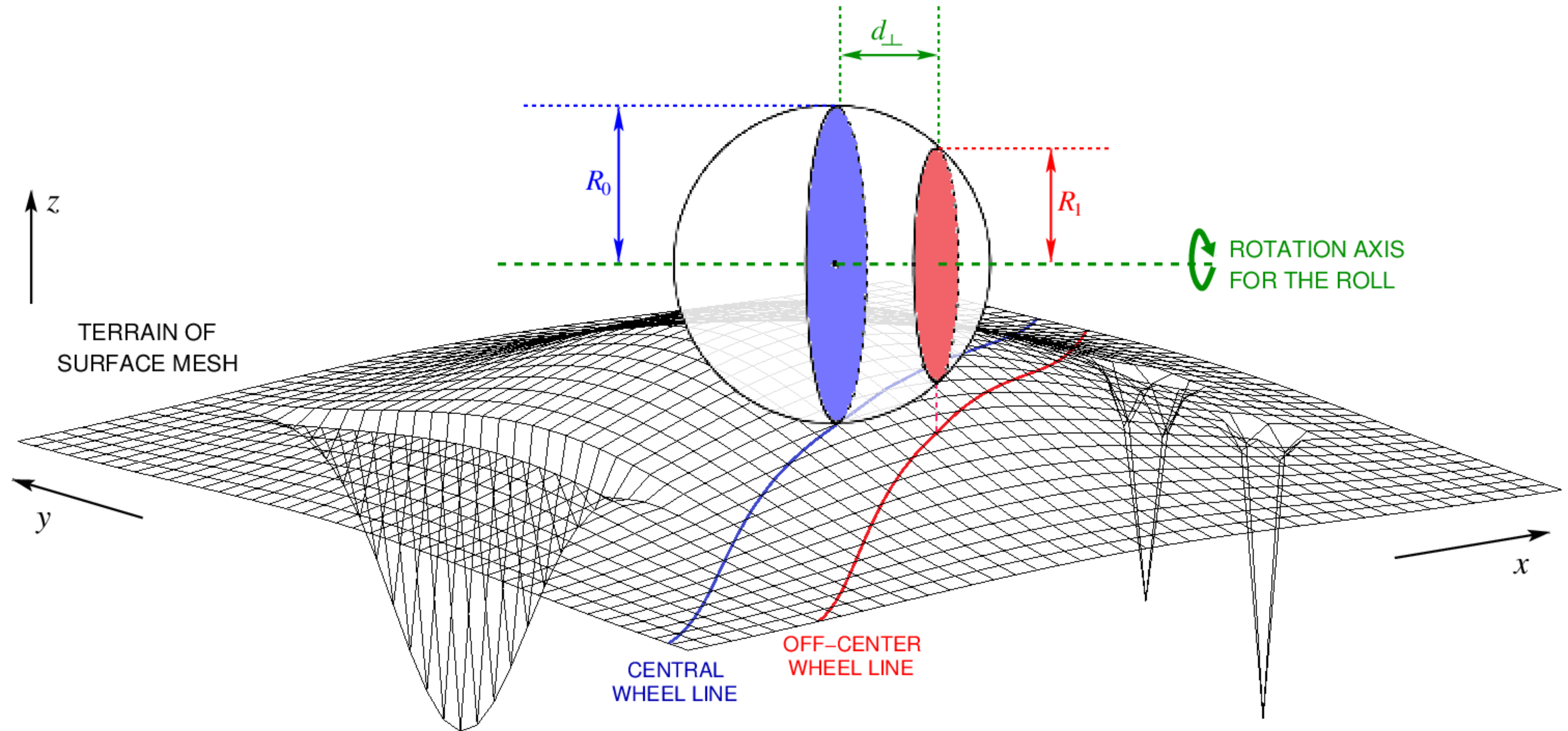


Figure 2.

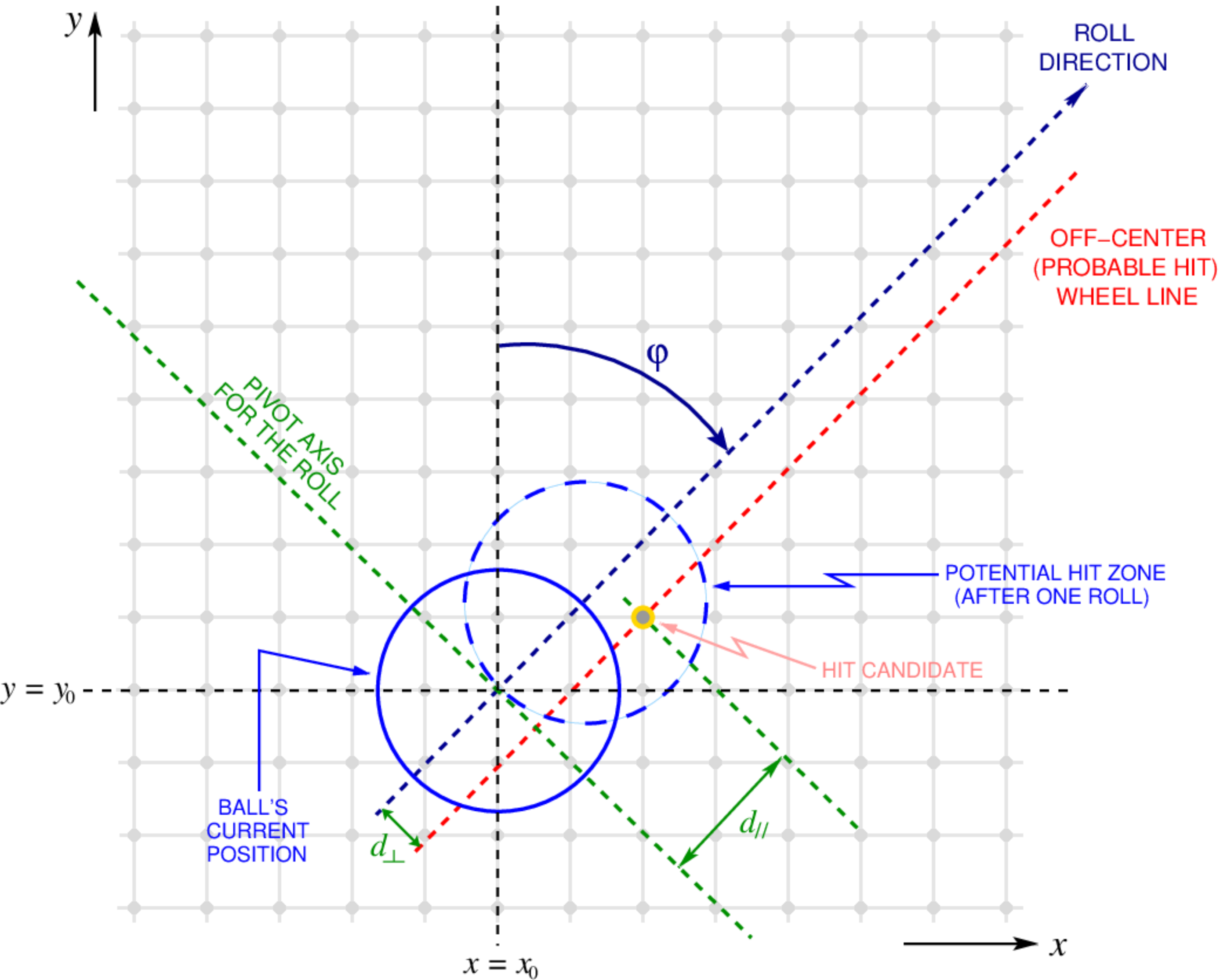


Figure 3.

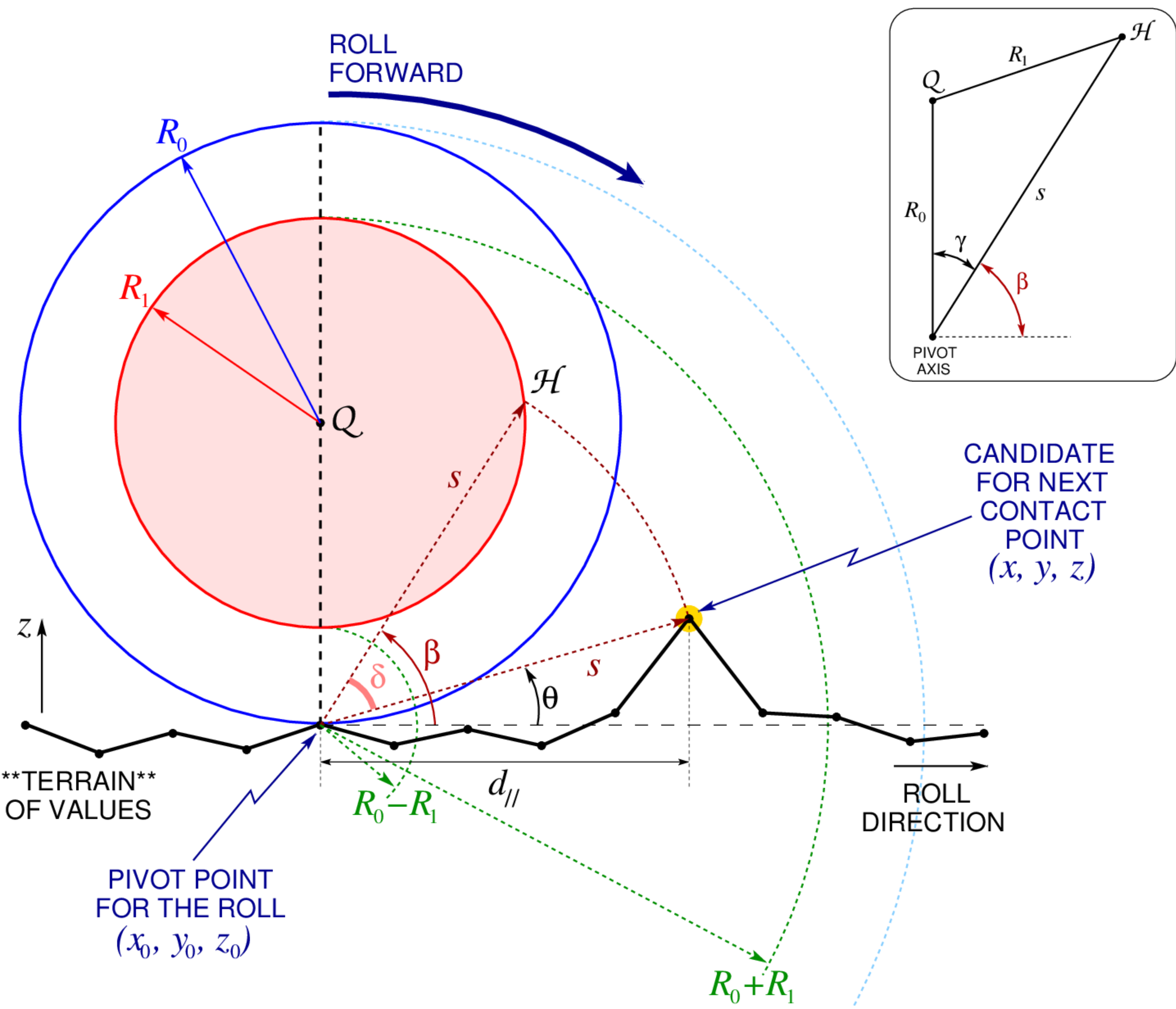


Figure 4.

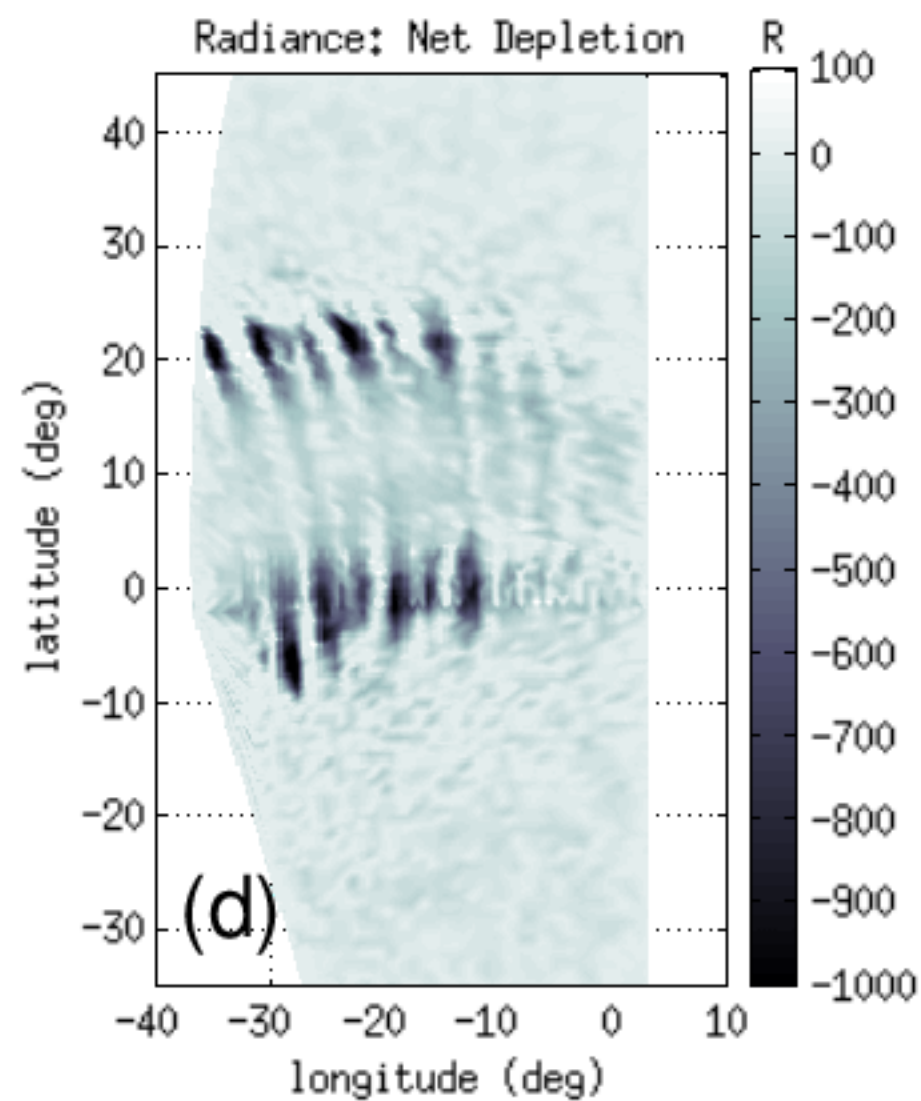
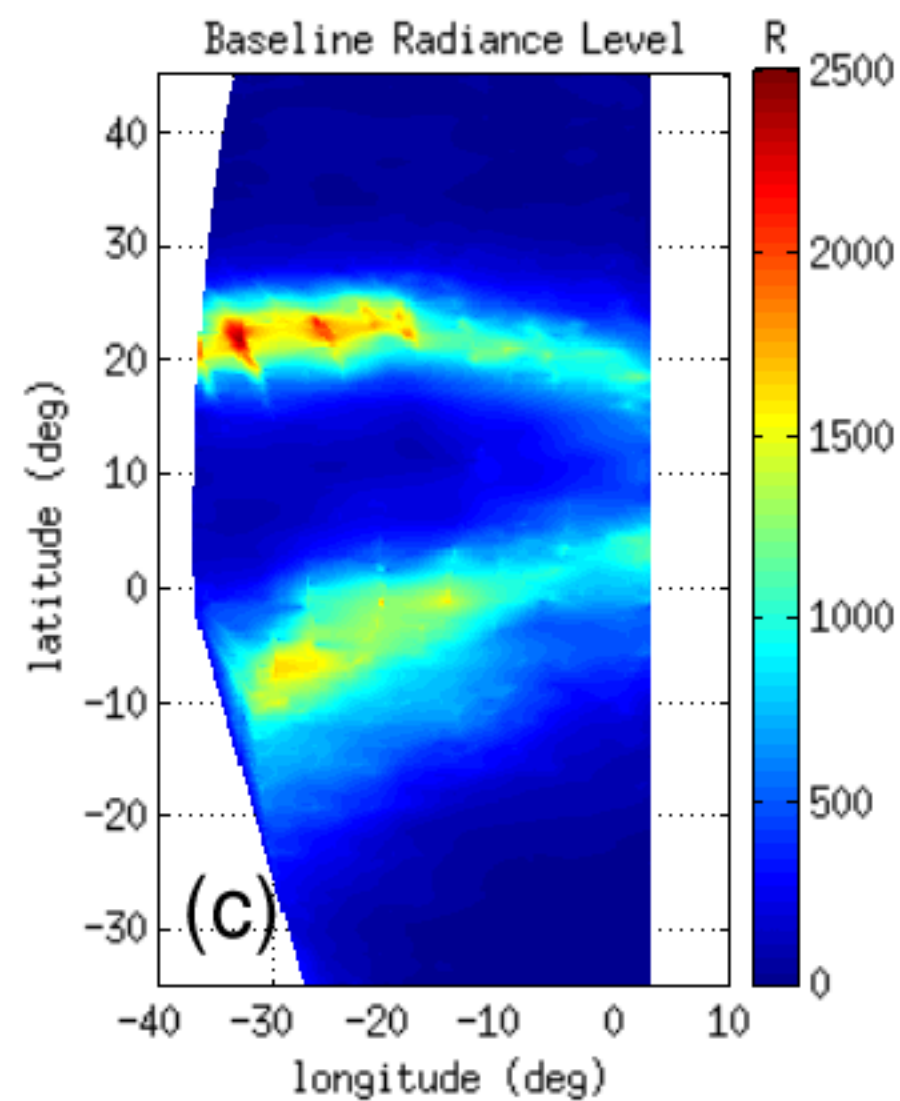
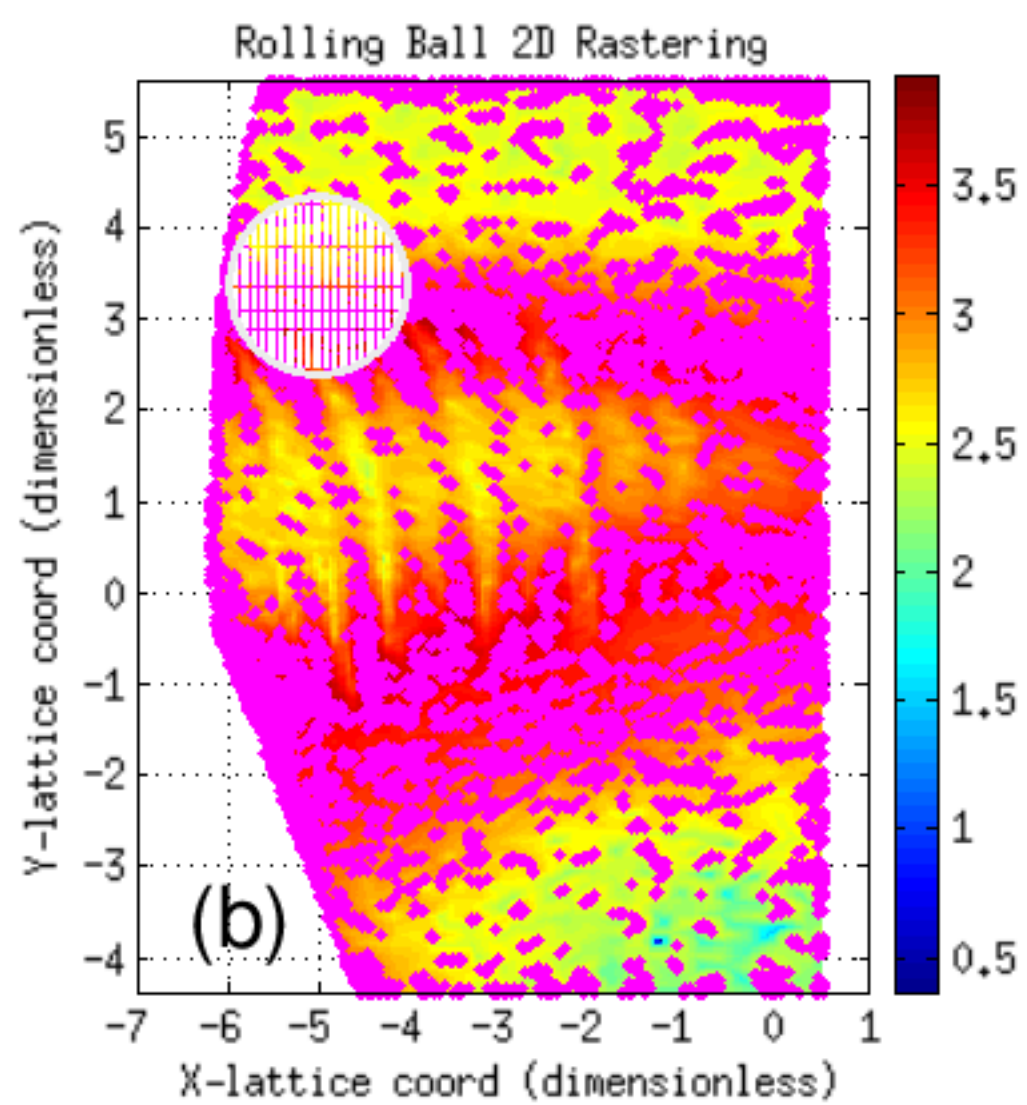
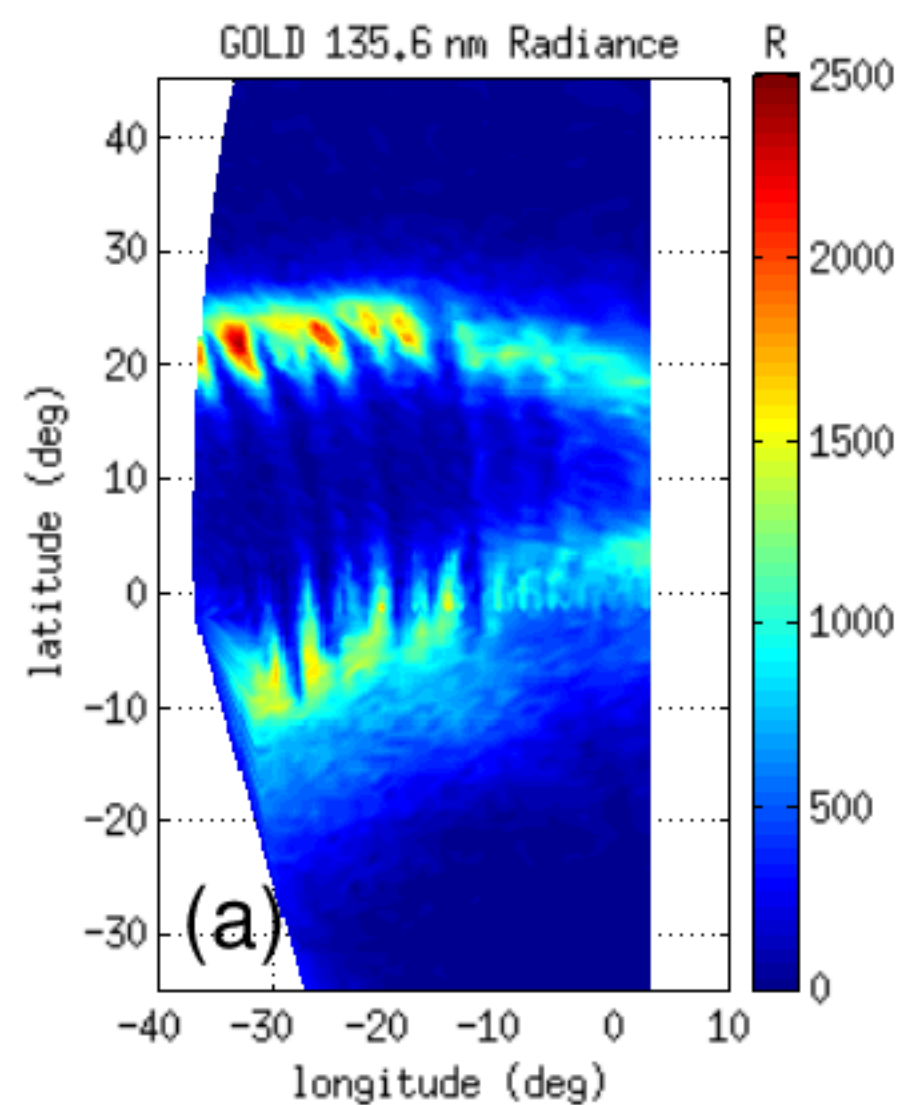


Figure 5.

